Thin Solid Films 603 (2016) 363–370

Contents lists available at ScienceDirect

Thin Solid Films

journal homepage: www.elsevier.com/locate/tsf

Control of crystal structure, morphology and optical properties of ceria films by post deposition annealing treatments

Asmaa Eltayeb [a,*], Rajani K. Vijayaraghavan [a], Anthony P. McCoy [b], Joseph Cullen [c], Stephen Daniels [a], Enda McGlynn [c]

[a] School of Electronic Engineering, National Centre for Plasma Science and Technology, Dublin City University, Glasnevin, Dublin 9, Ireland
[b] School of Physical Sciences, Dublin City University, Glasnevin, Dublin 9, Ireland
[c] School of Physical Sciences, National Centre for Plasma Science and Technology, Dublin City University, Glasnevin, Dublin 9, Ireland

ARTICLE INFO

Article history:
Received 16 February 2015
Received in revised form 18 February 2016
Accepted 19 February 2016
Available online 23 February 2016

Keywords:
Post-deposition annealing
Magnetron sputtering
X-ray photoelectron spectroscopy
UV–Vis absorption
Ceria
Microstructure
Grain shape
X-ray diffraction
Bandgap energy

ABSTRACT

In this paper, the effects of post-deposition annealing temperature and atmosphere on the properties of pulsed DC magnetron sputtered ceria (CeO_2) thin films, including crystalline structure, grain size and shape and optical properties were investigated. Experimental results, obtained from X-ray diffraction (XRD), showed that the prepared films crystallised predominantly in the CeO_2 cubic fluorite structure, although evidence of Ce_2O_3 was also seen and this was quantified by a Rietveld refinement. The anneal temperature and oxygen content of the Ar/O_2 annealing atmosphere both played important roles on the size and shape of the nanocrystals as determined by atomic force microscopy (AFM). The average grain size (determined by an AFM) as well as the out of plane coherence length (obtained from XRD) varied with increasing oxygen flow rate (OFR) in the annealing chamber. In addition, the shape of the grains seen in the AFM studies transformed from circular to triangular as the OFR was raised from 20 sccm to 30 sccm during an 800 °C thermal anneal. X-ray photoelectron spectroscopy was used to measure near-surface oxidation states of the thin-films with varying OFR in the annealing chamber. The bandgap energies were estimated from the ultra-violet and visible absorption spectra and low-temperature photoluminescence. An extracted bandgap value of 3.04 eV was determined for as-deposited CeO_2 films and this value increased with increasing annealing temperatures. However, no difference was observed in bandgap energies with variation of annealing atmosphere.

1. Introduction

Cerium oxides (CeO_2) have recently attracted much interest due to their chemical stability and unique chemical and physical properties, which make them suitable for many applications [1]. The valence of the Ce ion is very important in determining the structure of cerium oxides; trivalent Ce forms the sesquioxide Ce_2O_3 , which has a hexagonal lattice ($P\bar{3}$ *m1* space group), while tetravalent Ce forms CeO_2, commonly known as ceria, which has a cubic fluorite lattice (*Fm3m* space group) [2–4]. Thin films of the most common CeO_2 exhibit unique physical properties, such as a lattice constant similar to that of Si (α = 0.541 nm), a high refractive index and a high dielectric constant [5,6]. Hence, CeO_2 films are appropriate for many applications in optical devices [7,8], microelectronic devices [9,10], optoelectronic devices [11] and sensors [12]. They can also be utilised in other applications by effectively incorporating porosity between intermediate thin film layers to make thick porous structures. These further application areas include solar–thermal fuel generation [13], industrial catalysis [14,15], solid oxide fuel cells [16] and oxidation prevention of human cells in biomedical devices [17].

Since CeO_2 is stable even in sub-stoichiometric form ($CeO_{2-\delta}$), it has been produced by several growth techniques including electron-beam evaporation [18], chemical vapour deposition [10], ion-beam-assisted deposition [19,20], pulsed laser deposition [21] and reactive and non-reactive magnetron sputtering [6,13]. However, magnetron sputtering is one of the most attractive techniques for the preparation of CeO_2 films due to many advantages associated with the technique, including low substrate temperatures, scalability and good surface roughness characteristics [13], in addition to it being a well-established and relatively low cost industrial technique. Furthermore, the bipolar pulsed DC magnetron sputtering (PDCMS) process has attracted even greater attention recently because it shows higher deposition rates of defect-free ceramic films compared to conventional RF magnetron sputtering processes and therefore has potential as a commercially suitable method for large-area deposition of good quality ceramic films with high yield under diverse processing conditions [13].

According to various reports in the literature, highly crystalline CeO_2 can be obtained by applying heat to the substrate during deposition [22,23]. However, this can also be achieved by post-deposition annealing of

* Corresponding author.
E-mail address: asmaa.eltayeb2@mail.dcu.ie (A. Eltayeb).

http://dx.doi.org/10.1016/j.tsf.2016.02.036
0040-6090/

the CeO_2 film at high temperatures. Varying the substrate temperature during growth has an effect on the structural, chemical and optical properties but these effects are different to those obtained from varying oxygen flow rates (OFRs) during post-deposition annealing, especially in terms of microstructure (grain size and shape) of the films. Varying the post-deposition annealing temperature or the OFRs also results in changes in the concentration of oxygen vacancies, due to the altered thermodynamic equilibrium [24]. These factors can also influence the structure and morphology of CeO_2 films [25–27], which play an important role in solid/solid catalysis and the electrical properties of CeO_2 [28, 29] Thus varying OFRs and temperature during post-deposition annealing offers potential for control and engineering of a thin film properties.

In this work, we characterise CeO_2 thin films grown on Si(100) and quartz substrates grown by PDCMS using a CeO_2 target. The influence of varying the OFR and post-deposition annealing temperature on the deposit characteristics (microstructure and morphology, composition, optical properties etc.) was studied. The films were analysed by X-ray diffraction (XRD), atomic force microscopy (AFM), X-ray photoelectron spectroscopy (XPS), ultraviolet-visible (UV–Vis) spectroscopy and low-temperature photoluminescence (LPL). The influence of the post-deposition anneal temperature and variation of the OFRs on the PDCMS CeO_2 film properties have not been reported previously, and our work provides useful information on the effects of temperature and variation of OFRs in terms of controlling thin film properties, specifically grain shape and size.

2. Experimental

2.1. Material synthesis

Nanostructured CeO_2 thin films were prepared by PDCMS of a CeO_2 target onto silicon and quartz substrates (2×2 cm). The target was 99.99% pure cerium oxide (50 mm diameter and 6 mm thickness, supplied by the Kurt J. Lesker Company). Prior to deposition, the substrates were ultrasonically cleaned using acetone, a decontamination solution (30905 Aldrich), de-ionised water and blown dry with a nitrogen stream. An ENI RPG-100 pulse generator was used to drive a planar magnetron fitted with the CeO_2 target in power regulation mode. The chamber was first pumped down to a base pressure of 2×10^{-5} Pa by cryogenic pumping. The target was pre-sputtered for 10 min prior to deposition to reduce target surface contamination and to obtain a stable plasma density. Sputtering was carried out in a pure Ar atmosphere and the working pressure was adjusted and maintained at 0.7 Pa for the duration of the deposition. The target to substrate distance was adjusted to 6 cm. The sputtering was done at room temperature using a power of 65 W at 150 kHz without intentional heating. The substrates were at floating potential and the sputtering time was adjusted to 60 min to obtain a uniform film thickness of 50 ± 10 nm for all the deposited samples.

2.2. Annealing

After deposition and a short contact time with air at room temperature, the CeO_2 thin films samples were transferred into a quartz glass cell, where annealing treatments were performed. Samples were ramped up to target temperatures of 500 °C, 800 °C and 1000 °C at a rate (r) of 40 °C min^{-1} in an air ambient, and held at these temperatures for 1 h (the dwell time, t_d), in order to study the effect of annealing temperature on the film properties. An optimum temperature of 800 °C ($r = 40$ °C min^{-1}, $t_d = 1$ h) was chosen and further annealing experiments were carried out to study the effect of varying the oxygen partial pressure ($p(O_2)$) during annealing on the PDCMS deposited CeO_2 films. This was done by heating CeO_2 thin films deposits in an Ar/O_2 atmosphere with various OFR values at 800 °C, while keeping the argon flow rate (AFR) constant. The OFRs were varied in the range 0–50 sccm. After 1 h of annealing, the sample was allowed to cool down to room temperature (cooling time ≈ 30 min) before characterisation. Note that before each new annealing step, the gas atmosphere was refreshing by pumping and refilling.

2.3. Structure and morphology

The structural properties of the sputtered CeO_2 films were measured using a Bruker D8 advance X-ray diffractometer with CuK_α radiation of wavelength $\lambda = 1.54056$ Å to determine the crystallinity of the films. The XRD measurements were carried out in locked-coupled ($\theta - 2\theta$) mode in a 2θ range from 20° to 60°. A qualitative and quantitative phase analysis of the different phases was done by Rietveld analysis of the diffraction data using the FullProf program [30].

The surface morphology and roughness of the CeO_2 films were studied by a Veeco Nanoscope Dimension 3100 AFM instrument operating in tapping mode using aluminium-coated silicon (Si) probes (Budget Sensors, Tap300Al-G) with a tip radius of <10 nm. The intrinsic height resolution of the system is determined by the piezoelectric element and electronic noise and is ~0.4 nm, which provides a base level for measurement reliability. The surface roughness of each sample was determined as the root mean square (RMS) value R_q of the distribution of heights in the AFM topography images. The row/column statistical tool of Gwyddion software was used to calculate the standard deviation of R_q of all individual row/column values, and the values obtained were considered when determining the roughness error bars [31]. Where the calculated standard deviation of all individual row/column values is greater than the intrinsic height resolution of the system, the standard deviation is used as the error bar, and where it is less than the intrinsic height resolution, a value of 0.4 nm is used as the error bar.

2.4. Spectroscopy

XPS analysis was carried out using a VG Microtech electron spectrometer with a base pressure of 1×10^{-7} Pa. The photoelectrons were excited with a conventional Mg K_α ($h\nu = 1253.6$ eV) X-ray source and an electron energy analyser operating at a 20 eV pass energy, yielding an overall resolution of 1.2 eV. The samples were subjected to a mild degassing procedure in UHV at 300 °C in order to eliminate any surface contamination (this treatment was at too low a temperature to affect the properties being studied as a function of post deposition annealing), which may have arisen as a result of the transfer in atmosphere between the deposition and analysis chambers.

The optical absorption properties of the CeO_2 films were studied at room temperature using a Perkin Elmer Lambda 40 UV–Vis spectrometer in the range from 400 to 800 nm with a resolution of 4 nm. LPL measurements were carried out from 10 K to 22 K using a closed cycle helium cryostat system and a 325 nm excitation (He–Cd laser). The luminescence was analysed using a 1 m grating spectrometer (SPEX 1704) with a photomultiplier tube (Hamamatsu model R3310-02) in photon counting mode and cooled to −20 °C by a Peltier cooler (EMI FACT50).

3. Results & discussions

3.1. Structure and morphology

Fig. 1 shows a series of XRD θ–2θ patterns from the CeO_2 thin films: as-deposited and post-deposition annealed at temperatures of 500 °C, 800 °C and 1000 °C for 1 h in an air ambient. As seen in Fig. 1, the as-deposited CeO_2 films show a broad and featureless XRD pattern, characteristic of an amorphous structure. The CeO_2 films annealed at 500 °C shows the emergence of prominent diffraction peaks indexed to the cubic fluorite CeO_2 structure (PDF No. 00-034-0394), revealing that the CeO_2 films are being crystallized by the annealing process. For the films annealed at 800 °C and 1000 °C, we observe a higher intensity for the CeO_2 diffraction peaks which clearly reveals that the crystalline

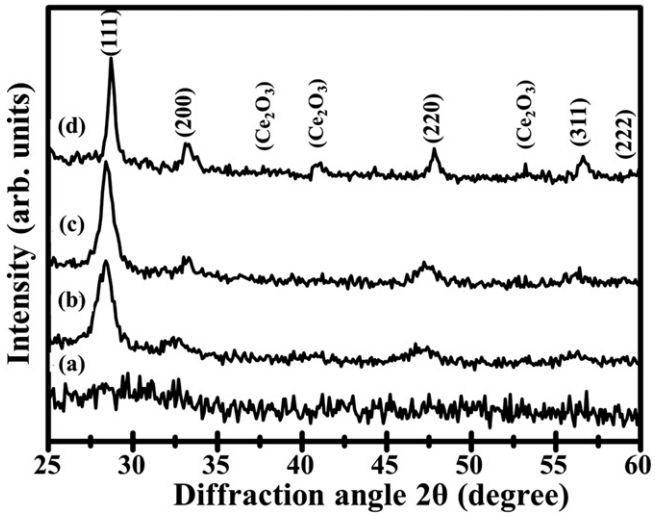

Fig. 1. XRD θ–2θ patterns of the CeO_2 films, (a) as-deposited and post-deposition annealed at temperatures of (b) 500 °C, (c) 800 °C and (d) 1000 °C in an air ambient.

fraction of the CeO_2 films is improved upon increasing the annealing temperature. At these temperatures several weak diffraction peaks corresponding to the Ce_2O_3 phase (PDF No. 00-049-1458) are also observed [32], possibly associated with the oxygen deficient growth environment (Ar gas only). These phases were further investigated using Rietveld refinement analysis of the CeO_2 diffraction patterns annealed at 500 °C and 800 °C and 1000 °C (shown in Fig. 1) provided some temperature dependent phase change information, but the main conclusion is that the deposit is mainly composed of cubic CeO_2, with some contribution from Ce_2O_3 in all samples, very possibly with a degree of localisation at the surface when the XPS data in the manuscript is considered in conjunction with the XRD data and Rietveld analysis [33,34]. The details of these impurity phases and their variation with annealing appear rather complex and, because of the evidence of surface localisation, further work will be needed to elucidate it more fully. Fig. 2 shows the analysis for the CeO_2 for the three temperatures (500 °C, 800 °C and 1000 °C). To refine the different phases, the structure model (space groups) Fm3m was used for CeO_2, CeO and Ce_2O_3, and $P\bar{3}ml$ for Ce_2O_3 (although no evidence of the CeO and hexagonal Ce_2O_3 phases were ultimately seen in the results of the refinement). Analysing the diffraction data it became obvious that some Ce_2O_3 impurity phase occurs in the 800 °C and 1000 °C samples, where there is evidence of the Ce_2O_3 cubic type structure however, this phase is present only in smaller concentrations (wt.%) of 7.5, 6.6 and 8.1 for 500 °C, 800 °C and 1000 °C, respectively. It can also be seen that the crystallinity deduced from the CeO_2 diffraction data improves with increasing temperature, by comparison of pattern (a) to (b) and (c) in Fig. 2. As stated above there was no evidence for the presence of any CeO impurities in any of the samples. The ratio of R_{wp}/R_{exp}, referred to as the goodness of fit (χ^2-factor) is reported in Table 1. For all annealed samples, the χ^2-factor is less than 1.5 indicating a high quality refinement [35]. However, in the XRD refinement of the samples annealed at 500 °C, not all peaks are well fitted/defined and this can be explained to be due to the fact that these samples contain both amorphous and crystalline fractions. Furthermore, the out of plane coherence length of the samples are reported in Table 1, obtained using the Rietveld refinement analysis. We have checked a selection of the out of plane coherence length values extracted from the Rietveld refinement analysis against estimates using the Debye-Scherrer formula applied to the full width at half maximum (FWHM) of the CeO_2 (111) XRD peak and found excellent agreement in all cases.

A series of XRD patterns showing the effect of OFR variation during post-deposition annealing on the crystallinity of the CeO_2 films are shown in Fig. 3. The OFRs ranges from 0 sccm to 50 sccm with a constant

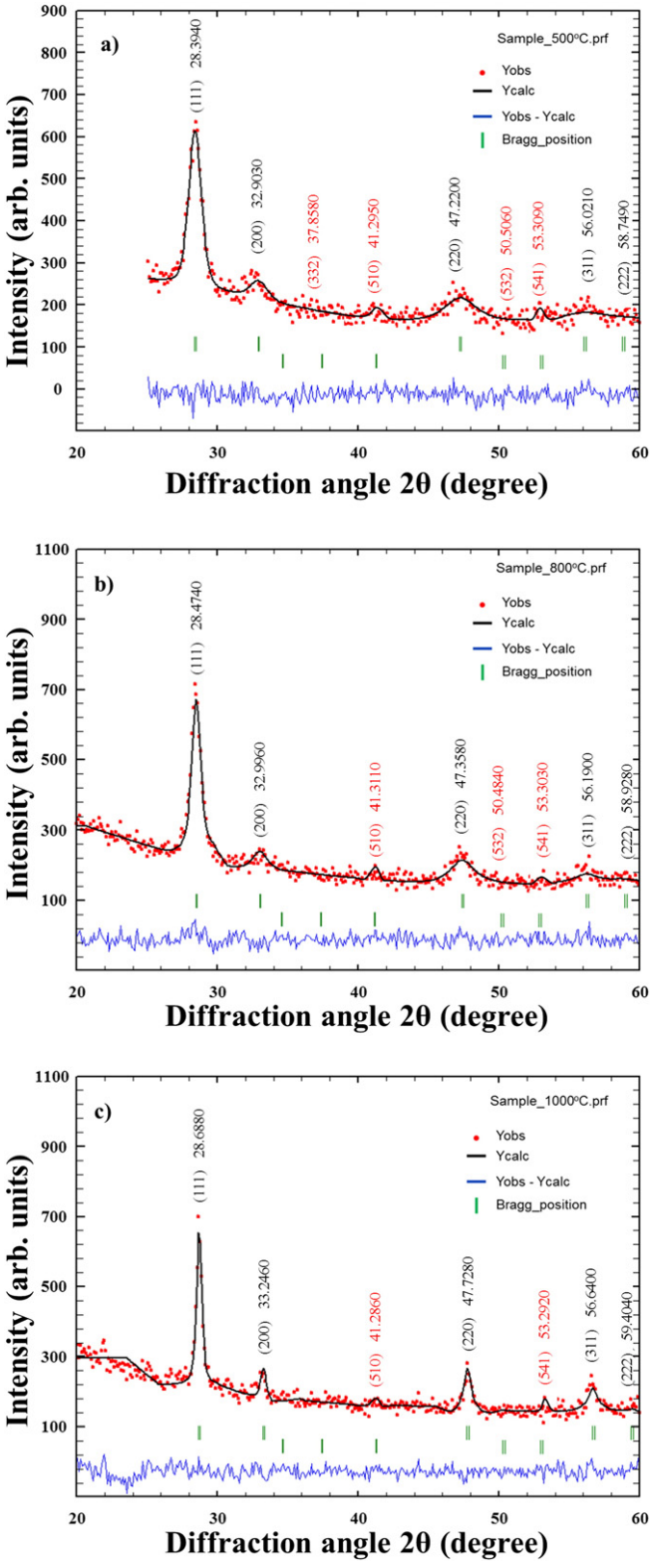

Fig. 2. Rietveld analysis of three diffraction patterns of CeO_2 annealed samples. a) 500 °C anneal, b) 800 °C anneal and c) 1000 °C anneal. The refinement of data was obtained using three different phases (CeO_2, Ce_2O_3; order corresponds to indicated Bragg peak positions from first to second line and we note that no evidence of the CeO phase is seen).

AFR of 50 sccm. The diffraction patterns for all samples are crystalline and clearly exhibit the presence of CeO_2 (111), (200), (220), (311) and (222) reflections. There are also weak diffraction peaks corresponding to the Ce_2O_3 phase.

Table 1
Rietveld refinement goodness of fit values and out of plane coherence length for CeO_2 samples annealed at 500 °C, 800 °C and 1000 °C.

Annealing temperature (°C)	Out of plane coherence length (nm)	Goodness of fit values (χ^2)
500	8	1.13
800	11	1.15
1000	19	1.23

Table 2
Summary of post-deposition annealing AFM and XRD results with variation in OFR. Samples were annealed at 800 °C for 1 h.

Sample	OFR (sccm)	FWHM (°)	Out of plane coherence length (nm)	RMS roughness (nm)	Grain shape
(a)	0	0.38	24	3.2 ± 1.2	Circular
(b)	10	0.38	24	2.8 ± 0.4	Circular
(c)	20	0.43	21	2.5 ± 0.8	Circular
(d)	30	0.53	17	1.0 ± 0.4	Triangular
(e)	40	0.46	20	2.3 ± 0.6	Triangular
(f)	50	0.38	24	5.2 ± 2.0	Triangular

The FWHMs determined from the Rietveld analysis are used as a measure of the crystalline quality of the CeO_2 crystallites and are reported in Table 2. As plotted in Fig. 4, the out of plane coherence length, based on the results from the Rietveld refinement analysis, decreases from 24 nm to 17 nm as the OFR increased from 0 sccm to 30 sccm, and increased to 24 nm as the OFR was raised further to 50 sccm. These values are all much less than the film thicknesses (which are constant in the range 50 ± nm as mentioned previously) and reveal a nanocrystalline deposit morphology. The oxygen content in the annealing chamber appears to have a small influence on the out of plane coherence length, which can also be correlated to the AFM images shown in Fig. 5, assuming the crystallites are approximately equiaxed, but the variation is close to limit of resolution of our XRD system.

The surface morphologies of the samples are investigated using an AFM. The plan-view AFM images for the surfaces of the CeO_2 films are presented in Fig. 5 for as-deposited films and films annealed at 800 °C in various OFRs (0 sccm, 20 sccm, 30 sccm and 50 sccm). As can be seen in Fig. 5(a), the as-deposited amorphous CeO_2 films have a very smooth and uniform surface. However, the surface morphology roughens after annealing at 800 °C, due to the crystallisation of the amorphous CeO_2 films. For samples annealed in OFRs of 0 sccm and 20 sccm (Fig. 5b and c), the shape of the CeO_2 grains is roughly circular and the RMS roughness values were 3.2 ± 1.2 nm to 2.5 ± 0.8 nm, respectively. By contrast, the grain shape for the samples annealed in OFRs of 30 sccm to 50 sccm (Fig. 5 d and e) is triangular in nature and the RMS roughness increased from 1.0 ± 0.4 nm to 5.2 ± 2.0 nm. The RMS roughness values (nm) of the films for a 2 × 2 μm^2 scan area are summarized in Table 2. For comparison, the as-deposited CeO_2 film RMS roughness is very smooth (at or below the intrinsic height resolution of the system, 0.4 nm).

3.2. Chemical composition studies using XPS

The chemical compositions of the films were studied by XPS in order to probe the presence of Ce^{4+} and Ce^{3+} oxidation states and their relative concentrations. Fig. 6 displays the Ce3d core level spectra of the as-deposited sample and samples annealed at 800 °C for 60 min in different OFRs. There was no significant effect from varying the OFRs in the annealing chamber. The established binding energy positions of the Ce^{3+} and Ce^{4+} oxidation state [36] are indicated by the vertical dotted lines [13]. The spectrum clearly shows a higher concentration of Ce in the Ce^{3+} oxidation state in the as-deposited sample compared to those annealed at 800 °C in gas, indicating a chemically reduced state of CeO_2 possibly associated with the oxygen deficient growth environment (Ar gas only). Thus the as-deposited CeO_2 sample shows a mixed phase Ce^{3+}/Ce^{4+} charge state, while the annealed CeO_2 samples in 0 sccm and 50 sccm OFRs are solely due to Ce^{4+} (within the limits of sensitivity of our system). It should be noted that although the presence of Ce^{3+} and Ce^{4+} could easily be identified in the Ce 3d as-deposited spectra, the relative concentrations could not be determined due to the complexity of the peak shape and the difficulty in fitting the peak.

Fig. 7 shows the corresponding O 1s XPS data for the as-deposited CeO_2 and CeO_2 annealed samples. The binding energy positions of the various Ce oxidation states in the O 1s core level spectra are almost identical and overlap considerably [37], mainly due to the O^{2-} nature of the oxygen atom in both Ce_2O_3 and CeO_2. These two contributions give rise to the feature labelled (i) in Fig. 7 and consequently, it is very difficult to deconvolve the O 1s peak into Ce_2O_3 and CeO_2 components. However, by assuming that the O 1s peak is in a single CeO_2 phase at the surface of the annealed samples due to the absence of a Ce^{3+} oxidation state in the Ce 3d data in Fig. 6, it was possible to establish peak fitting parameters for the O 1s CeO_2 Ce^{4+} component. These parameters were used to fit the O 1s spectrum for the as-deposited sample, where both Ce^{3+} and Ce^{4+} states exist as shown in the Ce 3d spectra in Fig. 6. It was evident that an additional peak was needed to achieve an adequate fit and it is suggested that this additional peak is due to the Ce^{3+} oxidation state and is separated from the Ce^{4+} by ~0.3 eV in

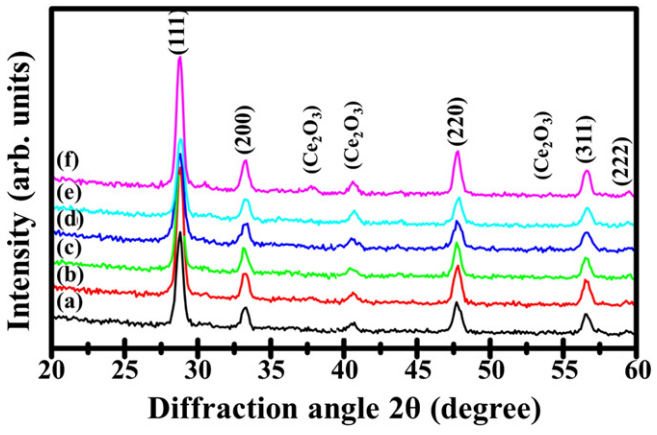

Fig. 3. XRD patterns of nanostructured CeO_2 thin films grown on Si(100) substrates. The films were annealed at 800 °C, with various (a) 0 sccm, (b) 10 sccm, (c) 20 sccm, (d) 30 sccm, e) 40 sccm and (f) 50 sccm.

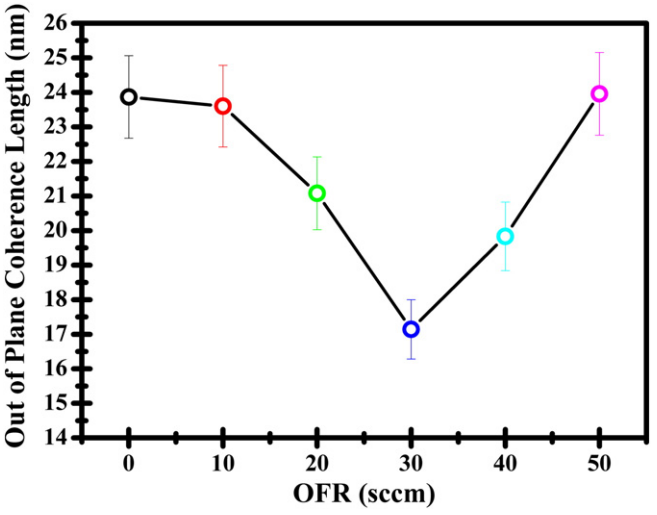

Fig. 4. Influence of OFR during post-deposition annealing on the out of plane coherence length of the CeO_2 films.

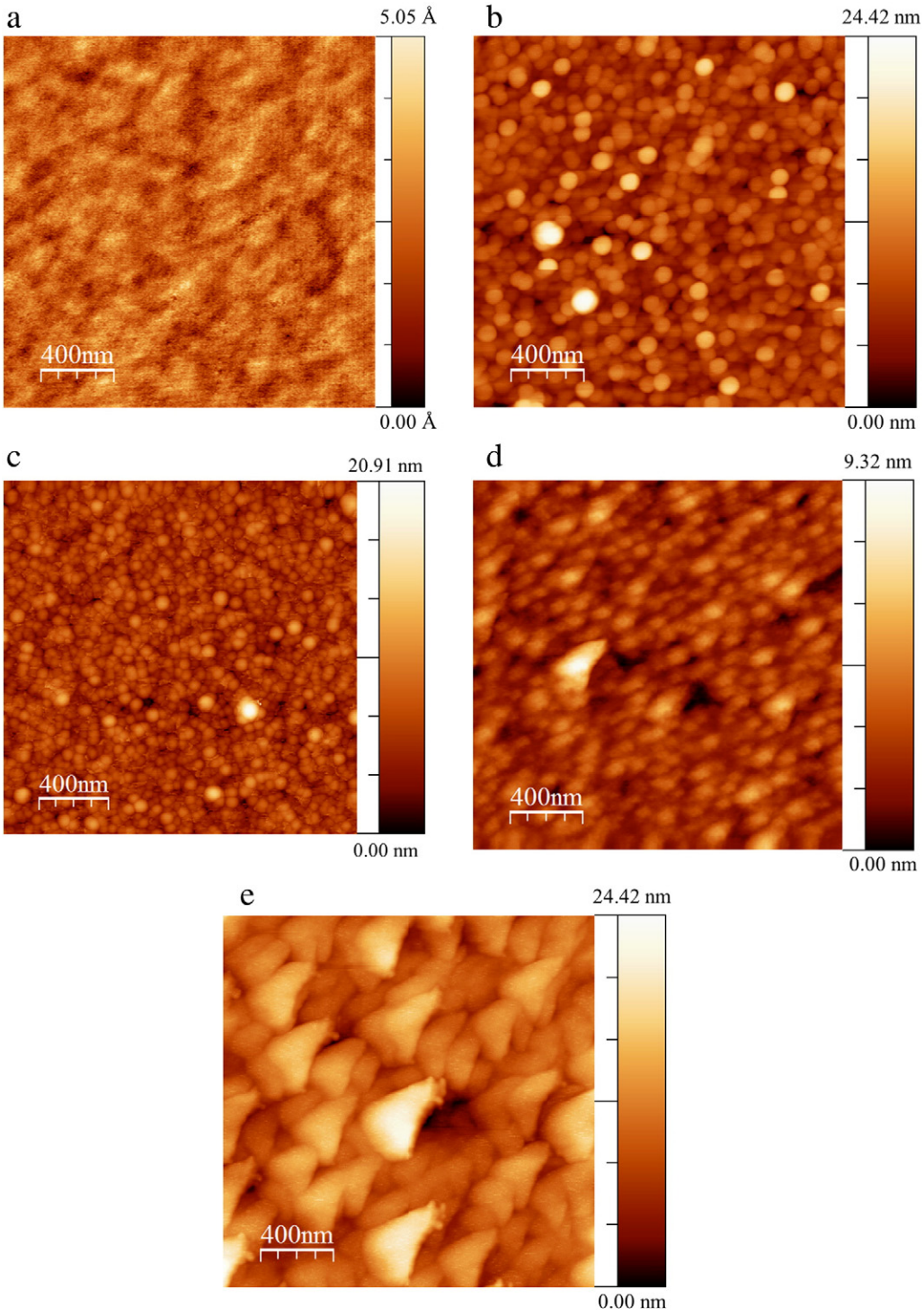

Fig. 5. 2 × 2 μm^2 plan-view AFM images of nanostructured CeO_2 films: (a) as-deposited and post-deposition annealed at 800 °C in an OFR of (b) 0 sccm, (c) 20 sccm, (d) 30 sccm and (e) 50 sccm. The AFR is kept constant at 50 sccm for all samples.

agreement with Mullins et al. [38]. Using these parameters the relative concentrations of the Ce^{3+}:Ce^{4+} as determined by the O 1s core level spectra in the as-deposited film is roughly 1:1.

The presence of OH groups or C–O contamination on the surface has previously been discussed as possible explanations for the feature labelled (ii) in Fig. 7, at a binding energy ~1.8 eV higher than that of the Ce^{4+} oxidation state in the O 1s spectrum [37,38]. Samples with exposure to different OFR conditions and samples annealed at a temperature of 800 °C contain larger relative contributions (up to ~31% of the signal in this spectral region) from these contaminant species. As stated above, the annealed samples, regardless of OFR, show evidence of Ce in the Ce^{4+} oxidation state only and a higher percentage of the contaminant feature (ii).

In Fig. 8, the annealed CeO_2 samples were further investigated by performing an off-normal emission scan. The scan indicated that the contaminant species O–H/C–O are indeed surface localised, as expected, and are most likely due to atmospheric exposure. All the samples were exposed to atmosphere at room temperature for a short period; thus it is possible that the surfaces of all samples were more heavily oxidised in contrast to the bulk at least within the sampling depth of the XPS, and

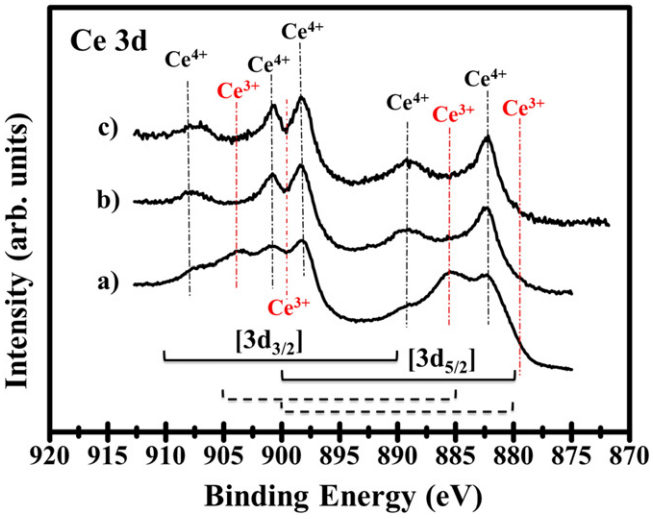

Fig. 6. XPS Ce3d core level spectra for a) as-deposited CeO_2 and 800 °C annealed CeO_2 samples with OFRs of b) 0 sccm and c) 50 sccm. The brackets show the spin orbital pairs (5/2) and (3/2) for Ce^{4+} (solid lines) and Ce^{3+} (dashed lines).

especially so for the case of some of the annealed samples. Lohwasser et al. [39] described an inward diffusion process of O_2 into CeO_2 sputtered films in the temperature range from 700 °C to 950 °C which results in CeO_δ material being surface localised, however due to the proximity of the various oxidation states in the O 1s spectra, it is very difficult to verify these findings using XPS in this study.

In summary, XPS indicates that the surface of the as-deposited film consisted of a Ce^{3+}/Ce^{4+} mixed phase, while the annealed sample surfaces appeared to contain just the Ce^{4+} oxidation state which is consistent with a more heavily oxidised surface for the annealed samples. It should be noted that XPS is extremely surface sensitive and its findings do not generally accurately reflect bulk properties. Nevertheless these XPS data are consistent with the XRD data and Rietveld refinement analysis above which show evidence only for Ce_2O_3 and CeO_2 phases, as XPS data from all samples shows the presence of only the Ce^{4+} and Ce^{3+} oxidation states (and no evidence for the Ce^{2+} charge state, associated with the CeO phase, which was not seen in XRD), though the relative concentrations indicated by XRD and XPS cannot be compared for the reason alluded to above.

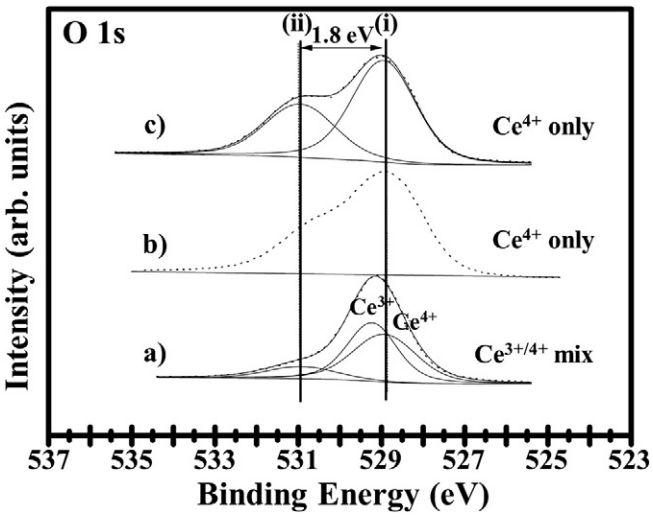

Fig. 7. O 1s XPS spectra of CeO_2 samples: a) as-deposited, and annealed at 800 °C in an OFR of b) 0 sccm and c) an OFR of 50 sccm.

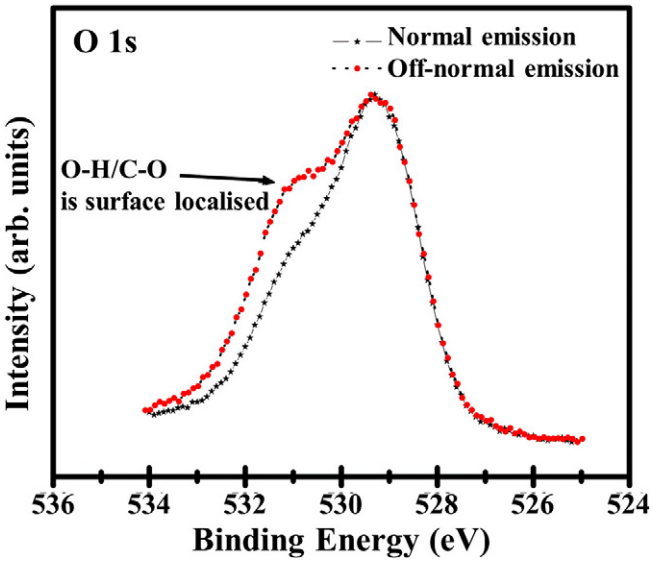

Fig. 8. O 1s XPS spectra of 800 °C thermal annealed CeO_2 sample (the data shown is from a sample annealed at an OFR value of 50 sccm, but essentially the same spectra and behaviour were seen regardless of OFR value for all samples annealed at 800 °C), normal emission and off-normal emission.

3.3. UV absorption and bandgap energy

It was previously reported [40–42] that a change in particle size due to exposure to different temperatures leads to a shift of absorption edge in UV–Vis absorption spectra. Fig. 9 shows the UV–Vis data from our samples, and the data indicates that the absorption edge shifts toward shorter wavelengths i.e. a blue shift, despite the increase in crystal size, with increasing post-deposition annealing temperature. The direct bandgap energy was estimated by extrapolating the absorption coefficient (α) from the absorbance data using a Tauc plot.

From the Tauc plot of $(\alpha h\nu)^2$ versus $h\nu$ (Fig. 10), one clearly sees that the extracted bandgap value increases from 3.3 eV to 3.6 eV as the annealing temperature increases from 500 °C to 1000 °C. For comparison the extracted bandgap value is 3.04 eV for as-deposited CeO_2 films. No changes were observed when the OFR was varied in the annealing chamber compared to the data from a sample annealed at 800 °C in air. The physical meaning of the extracted values and their variation with process conditions must however be treated with caution,

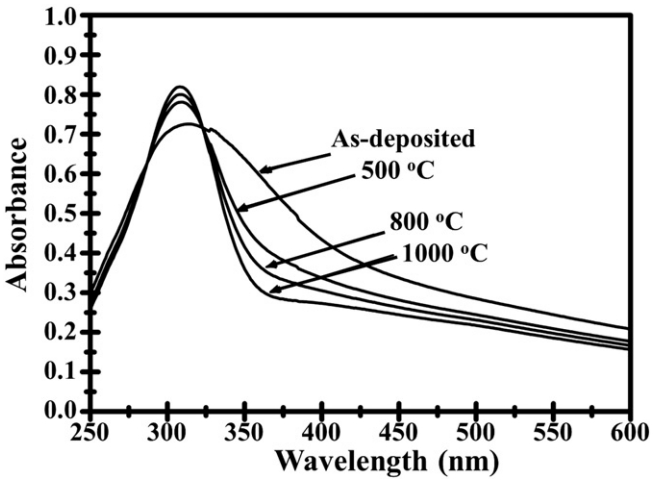

Fig. 9. UV–Vis absorption spectra of CeO_2 sputtered films, as-deposited and post-deposition annealed at temperatures of 500 °C, 800 °C and 1000 °C in an air ambient.

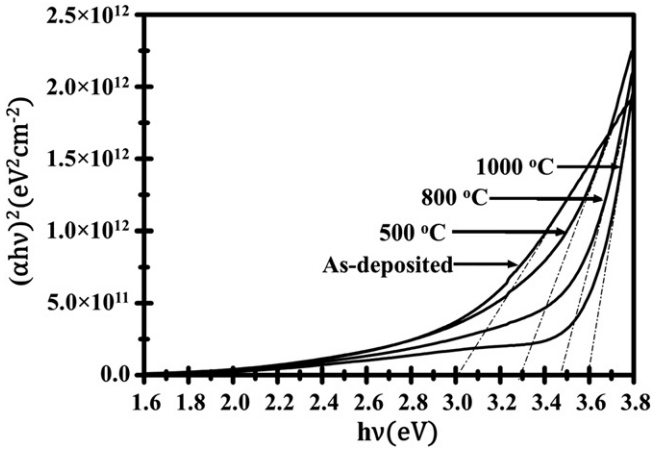

Fig. 10. Tauc plot of $(\alpha h\nu)^2$ vs. $h\nu$ for nanostructured CeO_2 sputtered films, as-deposited and post-deposition annealed at temperatures of 500 °C, 800 °C and 1000 °C in an air ambient.

because the influence of excitonic effects, as well as Urbach tail effects, on the spectra is not clear, and it is known that such effects are not accounted for within the Tauc plot formalism [43].

3.4. Photoluminescence

Low temperature photoluminescence was performed on nanocrystalline CeO_2 films annealed at 800 °C in various OFRs. All nanocrystalline CeO_2 samples displayed similar LPL spectra to that shown in Fig. 11, so only the data for a sample annealed in an OFR of 50 sccm is shown. It can be clearly seen that the peak intensity at 3.36 eV increases with increasing LPL measurement temperature. This behaviour indicates that the 3.36 eV emissions are associated with the films (unlike the laser plasma line at ~3.43 eV which doesn't vary with temperature). The emission at 3.36 eV is associated with near band edge emission from the film material and correlates well with the known value of the CeO_2 bandgap at room temperature (3.2 eV) [44,45], albeit being slightly larger due to the cryogenic measurement temperatures and associated bandgap increase. From our LPL data it does not appear that the bandgap is significantly affected by the OFR value during the annealing treatment, consistent with the UV–Vis data mentioned earlier.

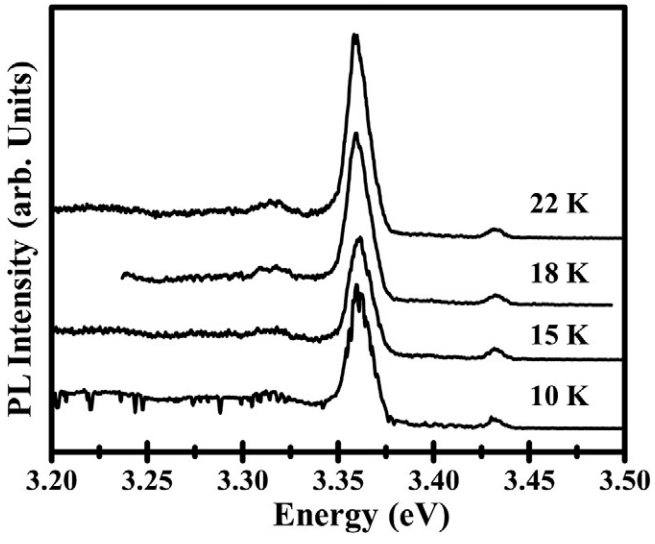

Fig. 11. LPL spectra of a nanocrystalline CeO_2 thin film annealed at 800 °C at an OFR of 50 sccm, measured at 10, 15, 18 and 22 Kelvin (K).

4. Conclusions

From the results presented above, the crystalline structure and morphology of CeO_2 thin films deposited by PDCMS are strongly dependent on the post-deposition annealing temperature and OFR of the Ar/O_2 annealing atmosphere. The average grain size can be controlled by either varying the annealing temperature or the OFR during the thermal anneal process. Raising the OFR from 20 sccm to 30 sccm resulted in the grain shape changing from roughly circular to triangular. Analysis of the chemical composition showed that the surfaces of the as-deposited films had contributions from both Ce^{3+} and Ce^{4+} charge states while the annealed CeO_2 films had contributions predominantly from the Ce^{4+} charge state and this charge state dominated at the film surface. These data are consistent with XRD data and Rietveld refinement analysis. The thermal anneal temperature also plays an important role in the optical properties of the films where an increase in temperature leads to a blue-shift and an increase in the bandgap value.

Our data and analysis clearly show that key materials properties such as the film nanomorphology, bandgap value and Ce ion charge state can be varied by a suitable thermal annealing treatment. These results may prove very useful in terms of enabling future materials and device development, with the aim of controlling key film parameters for technologically important applications, in particular in the areas of solar–thermal fuel generation and catalysis.

Acknowledgements

A. Eltayeb, S. Daniels and E. McGlynn specifically acknowledge postgraduate funding support from the INSPIRE Programme funded under the framework of the Irish Government's PRTLI Cycle 5, National Development Plan 2007–2014 with the assistance of the European Regional Development Fund.

References

[1] Y. Kuru, S. Bishop, J. Kim, B. Yildiz, H. Tuller, Chemomechanical properties and microstructural stability of nanocrystalline Pr-doped ceria: an in situ X-ray diffraction investigation, Solid State Ionics 193 (2011) 1–4.
[2] L. Wu, H. Wiesmann, A. Moodenbaugh, R. Klie, Y. Zhu, D. Welch, M. Suenaga, Oxidation state and lattice expansion of CeO_{2-x} nanoparticles as a function of particle size, Phys. Rev. B 69 (2004) 125415.
[3] E. Rossinyol, J. Arbiol, F. Peiró, A. Cornet, J. Morante, B. Tian, T. Bo, D. Zhao, Nanostructured metal oxides synthesized by hard template method for gas sensing applications, Sensors Actuators B Chem. 109 (2005) 57–63.
[4] N. Skorodumova, R. Ahuja, S. Simak, I. Abrikosov, B. Johansson, B. Lundqvist, Electronic, bonding, and optical properties of CeO_2 and Ce_2O_3 from first principles, Phys. Rev. B 64 (2001) 115108.
[5] N. Savvides, A. Thorley, S. Gnanarajan, A. Katsaros, Epitaxial growth of cerium oxide thin film buffer layers deposited by DC magnetron sputtering, Thin Solid Films 388 (2001) 177–182.
[6] M.-T. Ta, D. Briand, Y. Guhel, J. Bernard, J. Pesant, B. Boudart, Growth and structural characterization of cerium oxide thin films realized on Si (111) substrates by on-axis rf magnetron sputtering, Thin Solid Films 517 (2008) 450–452.
[7] R.P. Netterfield, W.G. Sainty, P.J. Martin, S.H. Sie, Properties of CeO_2 thin films prepared by oxygen-ion-assisted deposition, Appl. Opt. 24 (1985) 2267–2272.
[8] G. Atanassov, R. Thielsch, D. Popov, Optical properties of TiO_2, Y_2O_3 and CeO_2 thin films deposited by electron beam evaporation, Thin Solid Films 223 (1993) 288–292.
[9] T. Ami, M. Suzuki, MOCVD growth of (100)-oriented CeO_2 thin films on hydrogen-terminated Si (100) substrates, Mater. Sci. Eng. B 54 (1998) 84–91.
[10] D. Norton, J. Budai, M. Chisholm, Hydrogen-assisted pulsed-laser deposition of (001) CeO_2 on (001) Ge, Appl. Phys. Lett. 76 (2000) 1677–1679.
[11] A. Morshed, M. Moussa, S. Bedair, R. Leonard, S. Liu, N. El-Masry, Violet/blue emission from epitaxial cerium oxide films on silicon substrates, Appl. Phys. Lett. 70 (1997) 1647–1649.
[12] P. Jasinski, T. Suzuki, H.U. Anderson, Nanocrystalline undoped ceria oxygen sensor, Sensors Actuators B Chem. 95 (2003) 73–77.
[13] A. Eltayeb, R.K. Vijayaraghavan, A. McCoy, A. Venkatanarayanan, A.A. Yaremchenko, R. Surendran, E. McGlynn, S. Daniels, Control and enhancement of the oxygen storage capacity of ceria films by variation of the deposition gas atmosphere during pulsed DC magnetron sputtering, J. Power Sources 279 (2015) 94–99.
[14] A. Trovarelli, C. de Leitenburg, M. Boaro, G. Dolcetti, The utilization of ceria in industrial catalysis, Catal. Today 50 (1999) 353–367.
[15] T.X. Sayle, S.C. Parker, D.C. Sayle, Oxidising CO to CO_2 using ceria nanoparticles, Phys. Chem. Chem. Phys. 7 (2005) 2936–2941.
[16] B.C. Steele, A. Heinzel, Materials for fuel-cell technologies, Nature 414 (2001) 345–352.

[17] M.S. Wason, J. Colon, S. Das, S. Seal, J. Turkson, J. Zhao, C.H. Baker, Sensitization of pancreatic cancer cells to radiation by cerium oxide nanoparticle-induced ROS production, Nanomed. Nanotechnol. Biol. Med. 9 (2013) 558–569.
[18] M. Anwar, S. Kumar, F. Ahmed, N. Arshi, Y.J. Seo, C.G. Lee, B.H. Koo, Study of nanocrystalline ceria thin films deposited by e-beam technique, Curr. Appl. Phys. 11 (2011) S301–S304.
[19] D. Huang, F. Qin, Z. Yao, Z. Ren, L. Lin, W. Gao, Q. Ren, High quality CeO_2 film grown on Si (111) substrate by using low energy dual ion beam deposition technology, Appl. Phys. Lett. 67 (1995) 3724–3725.
[20] Y.M. Chiang, E. Lavik, I. Kosacki, H. Tuller, J. Ying, Defect and transport properties of nanocrystalline CeO_{2-x}, Appl. Phys. Lett. 69 (1996) 185–187.
[21] T. Chikyow, S. Bedair, L. Tye, N. El-Masry, Reaction and regrowth control of CeO_2 on Si (111) surface for the silicon-on-insulator structure, Appl. Phys. Lett. 65 (1994) 1030–1032.
[22] K.N. Rao, L. Shivlingappa, S. Mohan, Studies on single layer CeO_2 and SiO_2 films deposited by rotating crucible electron beam evaporation, Mater. Sci. Eng. B 98 (2003) 38–44.
[23] A. Khare, R. Choudhary, K. Bapna, D. Phase, S.P. Sanyal, Resonance photoemission studies of (111) oriented CeO_2 thin film grown on Si (100) substrate by pulsed laser deposition, J. Appl. Phys. 108 (2010) 103712.
[24] V.F. Solovyov, T. Ozaki, A. Atrei, L. Wu, A. Al-Mahboob, J.T. Sadowski, X. Tong, D. Nykypanchuk, Q. Li, Highly efficient solid state catalysis by reconstructed (001) ceria surface, Sci. Rep. 4 (2014) 4627.
[25] G. Chiodelli, L. Malavasi, V. Massarotti, P. Mustarelli, E. Quartarone, Synthesis and characterization of $Ce_{0.8}Gd_{0.2}O_{2-y}$ polycrystalline and thin film materials, Solid State Ionics 176 (2005) 1505–1512.
[26] H. Fukuda, M. Miura, S. Sakuma, S. Nomura, Structural and electrical properties of crystalline CeO_2 films formed by metalorganic decomposition, Jpn. J. Appl. Phys. 37 (1998) 4158.
[27] J.-H. Yoo, S.-W. Nam, S.-K. Kang, Y.-H. Jeong, D.-H. Ko, J.-H. Ku, H.-J. Lee, A study on the microstructure and electrical properties of CeO_2 thin films for gate dielectric applications, Microelectron. Eng. 56 (2001) 187–190.
[28] T. Suzuki, I. Kosacki, H.U. Anderson, Microstructure–electrical conductivity relationships in nanocrystalline ceria thin films, Solid State Ionics 151 (2002) 111–121.
[29] P. Miceli, S. Bensaid, N. Russo, D. Fino, CeO_2-based catalysts with engineered morphologies for soot oxidation to enhance soot-catalyst contact, Nanoscale Res. Lett. 9 (2014) 1–10.
[30] S. Schorr, A. Weber, V. Honkimäki, H.-W. Schock, In-situ investigation of the kesterite formation from binary and ternary sulphides, Thin Solid Films 517 (2009) 2461–2464.
[31] A.A. Duarte, S.L. Filipe, L.M. Abegão, P.J. Gomes, P.A. Ribeiro, M. Raposo, Adsorption kinetics of DPPG liposome layers: a quantitative analysis of surface roughness, Microsc. Microanal. 19 (2013) 867–875.
[32] J. Hanawalt, H. Rinn, L. Frevel, Chemical analysis by X-ray diffraction, Ind. Eng. Chem. Anal. Ed. 10 (1938) 457–512.
[33] C. Hardacre, G.M. Roe, R.M. Lambert, Structure, composition and thermal properties of cerium oxide films on platinum {111}, Surf. Sci. 326 (1995) 1–10.
[34] S. Eck, C. Castellarin-Cudia, S. Surnev, M. Ramsey, F. Netzer, Growth and thermal properties of ultrathin cerium oxide layers on Rh (111), Surf. Sci. 520 (2002) 173–185.
[35] R.A. Young, The rietveld method, Cryst. Res. Technol. 30 (1995).
[36] L. Garvie, P. Buseck, Determination of Ce^{4+}/Ce^{3+} in electron-beam-damaged CeO_2 by electron energy-loss spectroscopy, J. Phys. Chem. Solids 60 (1999) 1943–1947.
[37] H. Borchert, Y.V. Frolova, V.V. Kaichev, I.P. Prosvirin, G.M. Alikina, A.I. Lukashevich, V.I. Zaikovskii, E.M. Moroz, S.N. Trukhan, V.P. Ivanov, Electronic and chemical properties of nanostructured cerium dioxide doped with praseodymium, J. Phys. Chem. B 109 (2005) 5728–5738.
[38] D. Mullins, S. Overbury, D. Huntley, Electron spectroscopy of single crystal and polycrystalline cerium oxide surfaces, Surf. Sci. 409 (1998) 307–319.
[39] W. Lohwasser, J. Gerblinger, U. Lampe, H. Meixner, Effect of grain size of sputtered cerium-oxide films on their electrical and kinetic behavior at high temperatures, J. Appl. Phys. 75 (1994) 3991–3999.
[40] H.-I. Chen, H.-Y. Chang, Synthesis of nanocrystalline cerium oxide particles by the precipitation method, Ceram. Int. 31 (2005) 795–802.
[41] C. Liu, Z. Xu, Y. Zhang, J. Fu, S. Zang, Y. Zuo, Effect of annealing temperature on properties of ZnO: Al thin films prepared by pulsed DC reactive magnetron sputtering, Mater. Lett. 139 (2015) 279–283.
[42] P. Patsalas, S. Logothetidis, L. Sygellou, S. Kennou, Structure-dependent electronic properties of nanocrystalline cerium oxide films, Phys. Rev. B 68 (2003) 035104.
[43] C.F. Klingshirn, Semiconductor optics, Springer Science & Business Media, 2012.
[44] A. Corma, P. Atienzar, H. Garcia, J.-Y. Chane-Ching, Hierarchically mesostructured doped CeO_2 with potential for solar-cell use, Nat. Mater. 3 (2004) 394–397.
[45] Z.C. Orel, B. Orel, Optical properties of pure CeO_2 and mixed CeO_2/SnO_2 thin film coatings, Phys. Status Solidi B 186 (1994) K33–K36.